flow line, reaching a minimum of 0.7 cm yr^{-1} at Vostok station. Along the eastern shoreline a significant increase in accretion rate to 2.9 cm yr^{-1} is necessary to produce the grounded accreted ice. It is possible that some of the accreted ice thickening along the eastern shoreline is the result of compressive flow and not accretion. The lower layers in the ice sheet (3,300–2,800 m) undergo a 7% thickening, in contrast to the shallower layers of the ice sheet (2,400–1,900 m) which thin by 5–13% when grounding. The accretion process is most evident along the lake shorelines.

In the grounded ice adjacent to the southeastern Lake Vostok shoreline, we observe an average of 295 m of accreted ice in 21 radar profiles (Fig. 1, inset). No accretion ice is imaged adjacent to the eastern grounding line in the northern 15 radar profiles. We estimate the ice flux out of the lake, projected onto a 165-km line downslope of the lake, parallel to local contours. Assuming an average thickness of 295 m of accretion ice and a mean velocity of 3 m yr^{-1}, we estimate an annual accreted ice volume flux of 0.146 km^3 yr^{-1} along this line. For a lake volume[14] of 1,800 km^3, the residence time is 13,300 years. Previous estimates of residence time range from 4,500 years (ref. 6) to 125,000 years (ref. 1). The lower estimate (4,500 years), derived from the He^4/He^3 ratio[6], may be related to the formation of the accreted ice samples along the western shoreline in regions isolated from the main lake circulation—that is, the shallow embayment or the western grounding line. Deeper samples of accreted ice should be more representative of the open lake.

In the southern portion of Lake Vostok, the interaction between the lake and the overlying ice sheet is dominated by accretion. Earlier evidence for melting in this region[4] was based on radar data oblique to the ice flow field, and is, we believe, incorrect. Ice flow over southern Lake Vostok has a strong along-lake component, and has had a consistent orientation for the past 16,000 years—assuming that the velocity has been constant over this time period. The accretion process dominates at the lake shorelines, although some accretion continues over the middle of the lake. The accretion ice is generally transported out of the lake along the southeastern lake margin. Most samples of accretion ice analysed to date are derived either from the shallow embayment or from the western grounding line, environments that are not representative of the open lake system. □

Received 29 August 2001; accepted 11 February 2002.

1. Kapitsa, A. P., Ridley, J. K., Robin, G. de Q., Siegert, M. J. & Zotikov, I. A. A large freshwater lake beneath the ice of central East Antarctica. *Nature* **381,** 684–686 (1996).
2. Karl, D. M. *et al.* Microorganisms in the accreted ice of Lake Vostok, Antarctica. *Science* **286,** 2144–2147 (1999).
3. Priscu, J. C. *et al.* Geomicrobiology of subglacial ice above Lake Vostok, Antarctica. *Science* **286,** 2141–2144 (1999).
4. Siegert, M. J., Kwok, K., Mayer, C. & Hubbard, B. Water exchange between the subglacial Lake Vostok and the overlying ice sheet. *Nature* **403,** 643–646 (2000).
5. Jouzel, J. *et al.* More than 200 meters of lake ice above subglacial Lake Vostok, Antarctica. *Science* **286,** 2138–2141 (1999).
6. Jean-Baptiste, P., Petit, J.-R., Lipenkov, V. Y., Raynaud, D. & Barkov, N. I. Constraints on hydrothermal processes and water exchange in Lake Vostok from helium isotopes. *Nature* **411,** 460–462 (2001).
7. Siegert, M. J. *et al.* Physical, chemical and biological processes in Lake Vostok and other Antarctic subglacial lakes. *Nature* **414,** 603–609 (2001).
8. Popov, S. V., Mironov, A. V. & Sheremetiev, A. N. Average of the electromagnetic wave propagation velocity in ice measurements in Vostok station vicinity. *Materialy Glyatsiologicheskikh Issledovanii (Data of Glaciological Studies)* **90,** 206–208 (2001).
9. Popkov, A. M., Kudryavtsev, G. A., Verkulich, S. R., Masolov, V. N. & Lukin, V. V. in *International Workshop on Lake Vostok Study: Scientific Objectives and Technological Requirements* 26 (Arctic and Antarctic Research Institute, St Petersburg, Russia, 1998).
10. Whillans, I. M. Radio-echo layers and the recent stability of the West Antarctic ice sheet. *Nature* **264,** 152–155 (1976).
11. Fujita, S. *et al.* Nature of radio echo layering in the Antarctic ice sheet detected by a two-frequency experiment. *J. Geophys. Res. B* **104,** 13013–13024 (1999).
12. Kwok, R., Siegert, M. J. & Carsey, F. D. Ice motion over Lake Vostok, Antarctica: constraints on inferences regarding the accreted ice. *J. Glaciol.* **46,** 689–694 (2000).
13. Carslaw, H. S. & Jaeger, J. C. *Conduction of Heat in Solids* 285 (Oxford Univ. Press, Oxford, 1959).
14. Wüest, A. & Carmack, E. A priori estimates of mixing and circulation in the hard-to-reach water body of Lake Vostok. *Ocean Model.* **2,** 29–43 (2000).
15. Jezek, K., Noltimier, K. & The RAMP Product Team. *RAMP AMM-1 SAR Image Mosaic of Antarctica* [digital media] (Alaska SAR Facility, Fairbanks; and the National Snow and Ice Data Center, Boulder, Colorado, 2001).

Acknowledgements

The ice-penetrating radar data were acquired by the US National Science Foundation's Support Office for Aerogeophysical Research (SOAR) located at the University of Texas. We acknowledge the contributions of the Vostok field team, including the SOAR team, the Kenn Borek flight crews and the Raytheon East Camp crew. Comments from C. Bentley, R. Alley, E. Waddington and M. Siegert were appreciated. RADARSAT satellite data was provided by the Canadian Space Agency. This work was supported by the US National Science Foundation.

Competing interests statement

The authors declare that they have no competing financial interests.

Correspondence and requests for materials should be addressed to R.E.B. (e-mail: robinb@ldeo.columbia.edu).

Development of anisotropic structure in the Earth's lower mantle by solid-state convection

Allen K. McNamara*, Peter E. van Keken* & Shun-Ichiro Karato†

* *Department of Geological Sciences, University of Michigan, Ann Arbor, Michigan 48109-1063, USA*
† *Department of Geology and Geophysics, Yale University, New Haven, Connecticut 06520-8109, USA*

Seismological observations reveal highly anisotropic patches at the bottom of the Earth's lower mantle, whereas the bulk of the mantle has been observed to be largely isotropic[1–4]. These patches have been interpreted to correspond to areas where subduction has taken place in the past or to areas where mantle plumes are upwelling, but the underlying cause for the anisotropy is unknown—both shape-preferred orientation of elastically heterogenous materials[5] and lattice-preferred orientation of a homogeneous material[6–8] have been proposed. Both of these mechanisms imply that large-strain deformation occurs within the anisotropic regions, but the geodynamic implications of the mechanisms differ. Shape-preferred orientation would imply the presence of large elastic (and hence chemical) heterogeneity whereas lattice-preferred orientation requires deformation at high stresses. Here we show, on the basis of numerical modelling incorporating mineral physics of elasticity and development of lattice-preferred orientation, that slab deformation in the deep lower mantle can account for the presence of strong anisotropy in the circum-Pacific region. In this model—where development of the mineral fabric (the alignment of mineral grains) is caused solely by solid-state deformation of chemically homogeneous mantle material—anisotropy is caused by large-strain deformation at high stresses, due to the collision of subducted slabs with the core–mantle boundary.

Lattice-preferred orientation (LPO) leads to the development of a mineral fabric in material that deforms primarily by dislocation creep. Previous work[9] has shown that slabs cause high-stress regions in the lower mantle, which leads to localized regions of dislocation creep within a lower mantle dominated by diffusion creep under a wide range of rheological parameters. It has also been shown that hot, upwelling regions are low stress, and are therefore dominated by diffusion creep. The presence of dislocation creep is not in itself a

sufficient condition for the formation of LPO in slabs. In addition, the strain due to the dislocation creep must be greater than 100–200%. Here we investigate the circumstances under which this condition is met by a combined mineral-physics and dynamical-modelling approach. This requires the use of a composite rheology formulation involving a combination of diffusion and dislocation creep deformation mechanisms.

We choose rheological parameters for the upper and lower mantle based on mineral-physics observations[10,11], resulting in a viscosity profile that generally increases with depth and includes an increase at the base of the transition zone. We also use a yield stress approach[12] in the upper regions of our model to form subducting slabs. We place strain tracers in slab regions above the transition zone to track the evolution of deformation. Given the uncertainties related to first-principles calculations of fabric development, such as the critical shear stresses associated with specific slip systems and the nature of dynamic recrystallization, we assume that strain may be used as a proxy for the development of mineral fabric. During dislocation creep, material flows by the slipping of specific glide planes, resulting in an oriented array of crystal axes and promoting fabric development. On the other hand diffusion creep occurs by the migration of atoms involving grain-boundary sliding, resulting in a random orientation of crystal axes and tending to destroy any pre-existing fabric. Therefore, we track strain only in regions dominated by dislocation creep. We compare the resulting strain field to mineral-physics deformation experiments in order to assess the expected seismic anisotropy.

The numerical calculations of mantle convection are solved using the conservation equations of mass, momentum and energy in the extended Boussinesq formulation[13] using a finite-element approach. The modelling geometry is a two-dimensional quarter-cylinder with free-slip boundaries. We employ depth-dependent thermal expansivity and thermal conductivity[14,15]. We allow our convection calculations to run for long enough to ensure that the initial condition does not affect the results. Details of the model setup and rheological formulation are given in previous work[9]. Parameters used for the calculations presented here are given in Table 1.

Lagrangian finite strain is calculated as a post-processing step, using the velocity fields at each time step of the convection calculation. Strain is calculated for particles within regions dominated by dislocation creep by time-integrating the deformation gradient tensor for each strain tracer[16]. The strain calculation code was checked by comparison to analytical solutions of simple and pure shear as well as a combination of the two[17]. If a strain tracer leaves the regime of dislocation creep, its recorded strain magnitude is decreased as a function of further material strain. We assume that LPO is destroyed after the material stretches further than twice its original length.

The results of two calculations are given here (Figs 1 and 2) to illustrate the insensitivity of our results to the amount of internal heating and to the scaling geometry. The calculations vary in terms of heating mode and radial scaling. Figure 1 shows results from a calculation in which the mantle is entirely bottom-heated and scaled to preserve the volume ratio of the Earth's upper and lower mantle. Figure 2 shows results from a calculation in which the mantle is heated by both internal and bottom heating (~50% each), and is scaled to preserve the surface area to volume ratio of the mantle in a spherical Earth. These scalings have been found to better approximate the heat and mass transfer of spherical models[18]. Both results yield heat flow and radial viscosity profiles that are consistent with observations[19,20].

Snapshots in time of the temperature and viscosity ratio fields are shown in Figs 1c–e and 2c–e. The viscosity ratio is defined as the ratio of the components corresponding to dislocation creep and diffusion creep. Regions in blue represent a positive ratio, indicating that they are dominated by diffusion creep. Red regions represent a negative ratio, indicating a domination of dislocation creep. Note that most of the upper mantle flows by dislocation creep. In contrast the interior of the upper-mantle slab flows primarily by diffusion creep, because the upper-mantle activation coefficients result in a transition stress that increases with decreasing temperature. Away from the slab region, lower-mantle flow is dominated by diffusion creep, particularly in the lowermost boundary region, where high temperatures lead to low viscosities and therefore low stresses.

Strain tracers are shown as points on the viscosity ratio fields. Superimposed on tracer points are vectors representing the finite

Table 1 Calculation parameters

Parameter	Description	Units	Value, Fig. 1	Value, Fig. 2
ΔT	Temperature drop across mantle	K	3,000	3,000
α_o	Reference thermal expansivity	K^{-1}	3×10^{-5}	3×10^{-5}
ρ_o	Reference density	$kg\,m^{-3}$	4,500	4,500
C_p	Specific heat	$J\,kg^{-1}\,K^{-1}$	1,250	1,250
h	Mantle thickness	m	2.8×10^6	2.8×10^6
k_o	Reference thermal conductivity	$W\,m^{-1}\,K^{-1}$	5.6	5.6
g	Gravitational constant	$m\,s^{-2}$	9.8	9.8
κ_o	Reference thermal diffusivity	$m^2\,s^{-1}$	10^{-6}	10^{-6}
Di	Dissipation number		0.5	0.5
d_{um}	Upper mantle grain size	mm	2.0	2.0
d_{lm}	Lower mantle grain size	mm	1.0	1.0
m	Grain size index		2.5	2.5
n	Power law index		3.0	3.0
$A_{diff-um+}$	Upper-mantle diffusion creep prefactor	$d_{um}^m\,Pa^{-1}\,s^{-1}$*	1.3276×10^{-13}	2.6551×10^{-14}
$A_{diff-lm+}$	Lower-mantle diffusion creep prefactor	$d_{um}^m\,Pa^{-1}\,s^{-1}$*	6.2230×10^{-14}	1.3276×10^{-13}
$A_{disl-um+}$	Upper-mantle dislocation creep prefactor	$Pa^{-n}\,s^{-1}$*	4.7295×10^{-13}	9.4590×10^{-14}
$A_{disl-um+}$	Lower-mantle dislocation creep prefactor	$Pa^{-n}\,s^{-1}$*	1.2446×10^{-29}	2.6551×10^{-29}
$g_{diff-um}$	Upper-mantle diffusion creep activation coefficient		17	17
$g_{diff-lm}$	Lower-mantle diffusion creep activation coefficient		10	10
$g_{disl-um}$	Upper-mantle dislocation creep activation coefficient		31	31
$g_{disl-lm}$	Lower-mantle dislocation creep activation coefficient		10	10
σ_d	Ductile yield stress	MPa	400	250
σ'_b	Brittle yield stress gradient	$MPa\,km^{-1}$	5.33	3.33
$R_{surface}$	Non-dimensional surface radius		1.67813	1.4292
R_{bottom}	Non-dimensional bottom radius		0.67813	0.4292
$R_{interface}$	Non-dimensional upper—lower mantle boundary radius		1.42	1.19
η_{max}	Non-dimensional maximum viscosity		1.0	1.0
η_{min}	Non-dimensional minimum viscosity		10^{-6}	10^{-6}

* Indices m and n are the grain size index and the power law index, respectively.

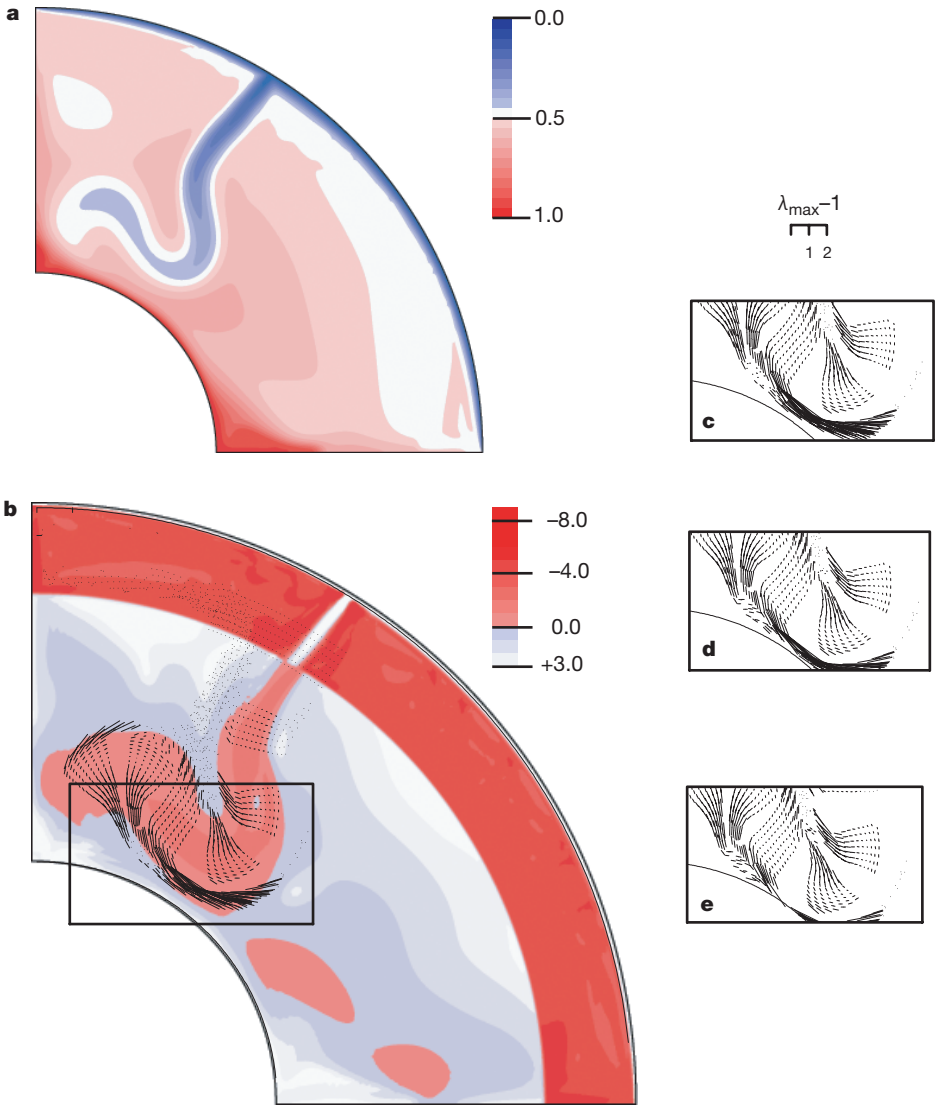

Figure 1 Snapshot of a slab impinging on the core-mantle boundary (CMB) in the bottom-heated model. **a**, Non-dimensional temperature field and **b**, ratio of viscosity due to dislocation creep over that due to diffusion creep. Positive values indicate deformation is dominated by diffusion creep, and negative values indicate deformation is dominated by dislocation creep. Superimposed are strain tracers and their associated strain vectors. Strain vectors represent maximum stretch, λ_{max}, and have a magnitude proportional to the stretch minus 1. The evolution of strain of the area of **b** shown in a box is given after successive intervals of 25 Myr in **c**, **d**, **e**.

strain. The vectors are in the direction of maximum principle strain, and have a length related to the stretch. The stretch is defined as the ratio of final length to the original length. Therefore, an undeformed particle has a stretch of unity. To differentiate better between strained and unstrained tracers the vector length is set to the stretch minus one, so only strained tracers have an associated vector.

To illustrate the temporal evolution of strain, Figs 1c–e and 2c–e show the strain configurations at successive times. Results from Fig. 1 reveal that although slab deformation in the lower mantle is dominated entirely by dislocation creep, the strain is not well developed because of low strain rates in the viscous slab. Directly above the core-mantle boundary (CMB), however, the magnitude of strain increases dramatically, resulting in a region of high strain that is directed laterally. Figure 1c–e reveals the time-dependent nature of the strain configuration. The overall strain magnitude in Fig. 1e is greatly reduced, and the directional sense is more random. Results are similar for the calculation shown in Fig. 2. Again, deformation in the slab is dominated by dislocation creep in a mantle otherwise dominated by diffusion creep. Figure 2b reveals a low magnitude lateral sense of strain directly above the CMB that increases with time (Fig. 2c–e) resulting in a strong laterally directed strain field. The strain markers also show that material is rotated as it approaches the upwellings that are constrained to the side boundaries of the model.

Our results show that the details of the strain field are time-dependent and can be quite complicated. Analysis of numerous convection results reveal that a lateral sense of high-magnitude extension (in excess of 100%) directly above the CMB is a general feature of the strain field. This feature tends to be long-lived but not permanent. As shown here, the strain pattern may decay into one that is characterized by a lower magnitude and inconsistent direction (that is, the progression from Fig. 1b–e). We also see that a coherent pattern of high-magnitude lateral strain tends to develop from a less developed state (that is, the progression

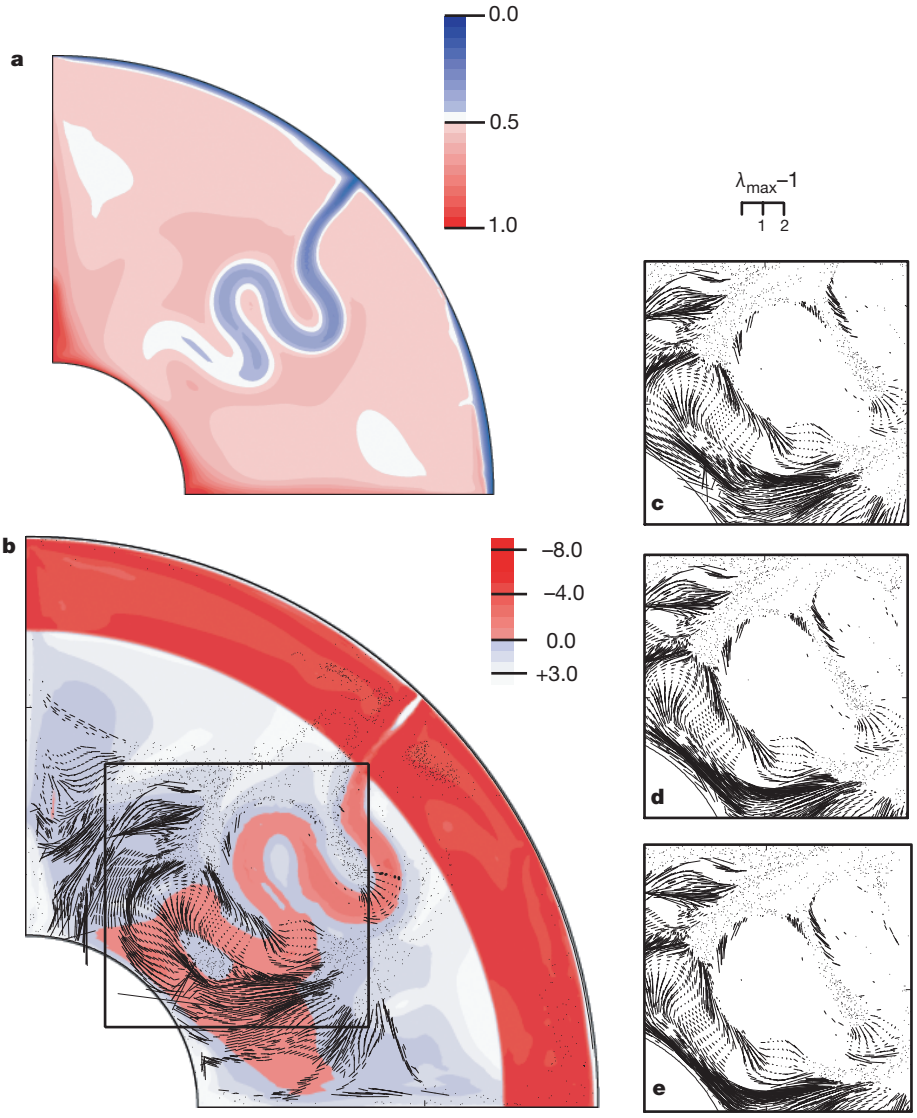

Figure 2 As Fig. 1, but for a model with bottom heating and internal heating.

from Fig. 2b–e). In general, we find that slab regions are characterized by a high degree of lateral strain directly above the CMB that occasionally reverts to a low-magnitude, more randomly oriented strain.

In order to assess the implications for seismic anisotropy, comparison to mineral-physics data is required. Experimental studies on LPO development show that the strength of LPO increases with strain, and reaches nearly steady-state values at a certain strain[21–23]. This critical strain depends on the material as well as deformation conditions. A detailed experimental study of LPO development is now available for (Mg, Fe)O (ref. 23). Because of its large elastic anisotropy[24], LPO of (Mg Fe)O results in a detectable seismic anisotropy (~1–2%)[5], although its volume fraction is small (less than 20%). For (Mg, Fe)O, a shear strain of ~200% is needed to develop significant LPO and steady-state LPO is formed at strains of ~400–500% (ref. 23). At steady state, LPO of (Mg, Fe)O corresponding to horizontal shear results in $V_{SH} > V_{SV}$ anisotropy[23] where V_{SH} and V_{SV} correspond to horizontal and vertical components of the shear wave velocity, respectively.

Our numerical models show the development of strong subhorizontal shear strain near the base of the mantle. Therefore, LPO of (Mg, Fe)O provides a natural explanation for the spatial variation in anisotropy in the lower mantle. Contributions from another major component, $(Mg, Fe)SiO_3$ perovskite, are difficult to estimate because of the absence of experimental data on LPO. In the two-phase mixture, (Mg, Fe)O is probably the weaker phase[10] and deforms more easily than $(Mg, Fe)SiO_3$. As a consequence, a higher degree of strain will occur in (Mg, Fe)O for a given deformation. In addition, if the results of LPO development in analogous material are used, the contribution from $(Mg, Fe)SiO_3$ perovskite is likely to be smaller than that of (Mg, Fe)O and the sense is opposite ($V_{SV} > V_{SH}$ for horizontal shear)[6,23]. Once materials leave high-stress regions, diffusion creep dominates and erases pre-existing LPO. Our models show highly time-dependent flow patterns, so the regions of strong anisotropy in these models correspond to regions with high-stress, large-strain deformation in the recent past. In contrast, if shape-preferred orientation due to laminated structures of palaeo-crust and ambient mantle is responsible for the anisotropy[5], then anisotropic structures will have much longer lifetimes and would not represent recent dynamic regimes. Also, the origin of the high contrast in elastic properties necessary for shape-preferred orientation is not clear. (We note that the origin of anisotropy in the Central Pacific, probably related to plume upwell-

ing, is not well constrained by the present work. It is possible that anisotropy in these regions is caused by shape-preferred orientation involving aligned melt pockets.)

Our results show that slabs are characterized by high stress, resulting in deformation dominated by dislocation creep within a mantle otherwise dominated by diffusion creep. We find complicated strain fields associated with deformation due to dislocation creep, but one consistent feature appears to be a large degree of laterally directed strain directly above the CMB. When examined in the context of mineral-physics experiments, we predict that this strain field results in significant seismic anisotropy, with $V_{SH} > V_{SV}$. This work shows that LPO of (Mg, Fe)O is a likely candidate for the seismic anisotropy observed near the CMB in slab regions. Although other processes may contribute to the formation of anisotropy[5], they are not required, and solid-state processes within a homogeneous material may suffice. □

Received 24 October 2001; accepted 31 January 2002.

1. Lay, T., Williams, Q. & Garnero, E. J. The core–mantle boundary layer and deep Earth dynamics. *Nature* **392,** 461–468 (1998).
2. Lay, T., Williams, Q., Garnero, E. J., Kellogg, L. & Wysession, M. E. in *The Core-Mantle Boundary* (eds Gurnis, M., Wysession, M. E., Knittle, E. & Buffett, B. A.) 299–318 (Geodynamics Series Vol. 28, Am. Geophys. Union, Washington DC, 1998).
3. Kendall, J. M. in *Earth's Deep Interior: Mineral Physics and Tomography from the Atomic to the Global Scale* (eds Karato, S., Forte, A. M., Liebermann, R. C., Masters, G. & Stixrude, L.) 133–159 (Geophysics Monograph 117, Am. Geophys. Union, Washington DC, 2000).
4. Ritsema, J. Evidence for shear velocity anisotropy in the lowermost mantle beneath the Indian Ocean. *Geophys. Res. Lett.* **27,** 1041–1044 (2000).
5. Kendall, J. M. & Silver, P. G. Constraints from seismic anisotropy on the nature of the lowermost mantle. *Nature* **381,** 409–412 (1996).
6. Karato, S. Some remarks on the origin of seismic anisotropy in the D″ layer. *Earth Planets Space* **50,** 1019–1028 (1998).
7. Karato, S. Seismic anisotropy in the deep mantle, boundary layers and the geometry of mantle convection. *Pure Appl. Geophys.* **151,** 565–587 (1998).
8. Stixrude, L. in *The Core-Mantle Boundary* (eds Gurnis, M., Wysession, M. E., Knittle, E. & Buffett, B. A.) 83–96 (Geodynamics Series Vol. 28, Am. Geophys. Union, Washington DC, 1998).
9. McNamara, A. K., Karato, S. & van Keken, P. E. Localization of dislocation creep in the lower mantle: Implications for the origin of seismic anisotropy. *Earth Planet. Sci. Lett.* **191,** 85–99 (2001).
10. Yamazaki, D. & Karato, S. Some mineral physics constraints on the rheology and geothermal structure of Earth's lower mantle. *Am. Mineral.* **86,** 385–391 (2001).
11. Frost, H. J. & Ashby, M. F. *Deformation Mechanism Maps* (Pergamon, Oxford, 1982).
12. Tackley, P. J. Self-consistent generation of tectonic plates in time-dependent, three-dimensional mantle convection simulations: 1. Pseudoplastic yielding. *Geochem. Geophys. Geosys.* [online] ⟨http://g-cubed.org/⟩ **1,** 2000GC000036 (2000).
13. Ita, J. & King, S. D. Sensitivity of convection with an endothermic phase change to the form of governing equations, initial conditions, boundary conditions, and equations of state. *J. Geophys. Res.* **99,** 15919–15938 (1994).
14. Jarvis, G. T. & McKenzie, D. P. Convection in a compressible fluid with infinite Prandtl number. *J. Fluid Mech.* **96,** 515–583 (1980).
15. Leitch, A. M., Yuen, D. A. & Sewell, G. Mantle convection with internal heating and pressure-dependent thermal expansivity. *Earth Planet. Sci. Lett.* **102,** 213–232 (1991).
16. Spencer, A. J. M. *Continuum Mechanics* (Longman, London, 1980).
17. Ramberg, H. Particle paths, displacement and progressive strain applicable to rocks. *Tectonophysics* **28,** 1–37 (1975).
18. van Keken, P. E. Cylindrical scaling for dynamical cooling models of the Earth. *Phys. Earth Planet. Inter.* **124,** 119–130 (2001).
19. Mitrovica, J. X. & Forte, A. M. Radial profile of mantle viscosity: results from the joint inversion of convection and postglacial rebound observables. *J. Geophys. Res.* **102,** 2751–2769 (1997).
20. Pollack, H. N., Hurter, S. J. & Johnson, J. R. Heat flow from the Earth's interior: analysis of the global data set. *Rev. Geophys.* **31,** 267–280 (1993).
21. Zhang, S. & Karato, S. Preferred orientation of olivine deformed in simple shear. *Nature* **375,** 774–777 (1995).
22. Mainprice, D., Barroul, G. & Ben Ismail, W. in *Earth's Deep Interior: Mineral Physics and Tomography from the Atomic to the Global Scale* (eds Katato, S. *et al.*) 237–264 (Am. Geophys. Union, Washington DC, 2000).
23. Yamazaki, D. & Karato, S. Fabric development in (Mg,Fe)O during large strain, shear deformation: Implications for seismic anisotropy in Earth's lower mantle. *Phys. Earth Planet. Inter.* (in the press).
24. Karki, B. B. *et al.* Structure and elasticity of MgO at high pressure. *Am. Mineral.* **82,** 51–60 (1997).

Acknowledgements

We thank M. Gurnis, D. Yamazaki, R. Wenk, T. Lay and B. Kiefer for discussions. This research was supported by the CSEDI program of the National Science Foundation.

Competing interests statement

The authors declare that they have no competing financial interests.

Correspondence and requests for materials should be addressed to A.K.M. (e-mail: mcnamar@umich.edu).

A ceratopsian dinosaur from China and the early evolution of Ceratopsia

Xing Xu*, Peter J. Makovicky†, Xiao-lin Wang*, Mark A. Norell‡ & Hai-lu You*

** Institute of Vertebrate Paleontology and Paleoanthropology, Chinese Academy of Sciences, Beijing, 100044, China*
† The Field Museum, 1400 S. Lake Shore Drive, Chicago, Illinois 60605, USA
‡ American Museum of Natural History, Central Park West at 79th St., New York 10024, USA

Ceratopsians (horned dinosaurs) represent one of the last and the most diverse radiations of non-avian dinosaurs[1–4]. Although recent systematic work unanimously supports a basal division of Ceratopsia into parrot-like psittacosaurids and frilled neoceratopsians, the early evolution of the group remains poorly understood, mainly owing to its incomplete early fossil record. Here we describe a primitive ceratopsian from China. Cladistic analysis posits this new species as the most basal neoceratopsian. This new taxon demonstrates that some neoceratopsian characters evolved in a more incremental fashion than previously known and also implies mosaic evolution of characters early in ceratopsian history.

The lacustrine lower part of the Yixian Formation of western Liaoning, China, has produced many spectacular fossil remains, including feathered dinosaurs[5]. Recently a number of important three-dimensionally preserved vertebrate fossils, including specimens of a new ceratopsian, have been collected from the fluvial facies that form the lowest part of the Yixian Formation[6]. Some radiometric analyses suggest these deposits are older than 128 Myr and younger than 139 Myr (ref. 5) (Early Cretaceous period) but others imply they are older than 145 Myr (ref. 7) (Late Jurassic period).

Ceratopsia Marsh, 1890
Neoceratopsia Sereno, 1986
Liaoceratops yanzigouensis gen. et sp. nov.

Etymology. The generic name is derived from the provincial name 'Liaoning', and the suffix 'ceratops', commonly used for horned dinosaur names. The specific name 'yanzigou' refers to the village near which the holotype was found.

Diagnosis. Neoceratopsian characterized by sutures between premaxilla, maxilla, nasal and prefrontal intersecting at a common point high on the side of the snout, possession of several tubercles on the ventra margin of the angular, a foramen on the posterior face of the quadrate near the articulation with the quadratojugal, a small tubercle on the dorsal border of the foramen magnum, and a thick posterior border of the parietal frill.

Holotype. IVPP (Institute of Vertebrate Paleontology and Paleoanthropology, Beijing) V12738, an almost complete skull (Fig. 1).

Referred specimen. IVPP V12633, a juvenile skull (Fig. 2).

Locality and horizon. Yanzigou and Lujiatun, Shangyuan, western Liaoning, China; the lowest part of the Yixian Formation, probably Early Cretaceous.

Description. The holotype skull of *Liaoceratops* is comparable in size to other basal ceratopsians such as *Psittacosaurus* and *Chaoyangsaurus*. Progressive, but incomplete, sutural closures between skull elements suggest that it derives from a subadult individual. The rostral appears unkeeled as in *Psittacosaurus*. As in many neoceratopsians, the rostral bears lateral processes along the buccal margin. The premaxilla forms much of the side of the snout and extends posterodorsally to reach the prefrontal, as in psittacosaurids and basal ornithopods. Three cylindrical premaxillary teeth are present as in the primitive neoceratopsian *Archaeoceratops*[8]. The snout is relatively wide in dorsal view, and tapers abruptly, being intermediate in form between that of psitta-